Direct Numerical Simulation of film boiling around a superheated sphere immersed in a subcooled liquid

Gauthier Bourdon, Sébastien Tanguy, Christophe Airiau

Highlights

Direct Numerical Simulation of film boiling around a superheated sphere immersed in a subcooled liquid

Gauthier Bourdon,Sebastien Tanguy,Christophe Airiau

- Film Boiling Simulation around a superheated solid
- Fully resolved vapor film
- Local results for film boiling in subcooled liquids
- Parametric Study on Heat Transfer

Direct Numerical Simulation of film boiling around a superheated sphere immersed in a subcooled liquid

Gauthier Bourdon[a], Sebastien Tanguy[a] and Christophe Airiau[a]

[a]IMFT, UMR 5502 CNRS-UPS-INPT, Université de Toulouse, France,

ARTICLE INFO

Keywords:
Film boiling
Heat Transfer
Subcooled liquid
Direct Numerical Simulation
Level Set/Ghost Fluid Method

ABSTRACT

Film boiling around immersed objects in a subcooled liquid is critical in various engineering applications and offer many scientific issues. After presenting a numerical solver able to simulate film boiling around a solid obstacle and some preliminary validations of this solver, we propose a comprehensive study based on the Direct Numerical Simulation (DNS) to investigate accurately on the dynamical and heat transfer effects inside the vapor film. After defining two Jakob numbers related respectively to the wall superheat and to the liquid, a parametric study is performed by varying both dimensionless numbers. The simulations allow to visualize the flow structure inside the vapor film and to predict angular variations of the local Nusselt number along the solid wall. In particular, spatial distributions of the local heat flux, related to variations of the film thickness along the solid obstacle, are observed with higher values at the bottom part of the sphere due to buoyancy effect. The simulations also provide accurate data on the global Nusselt number variation with respect to the Jakob numbers and confirm the dominance of conduction heat transfer inside the vapor film. Finally, the study also explores the equilibrium between vaporization and condensation processes which leads to the stabilization of the vapor film around the solid obstacle. This research enhances the understanding of subcooled film boiling and offers new data for film boiling model validation.

1. Introduction

The study of film boiling in subcooled conditions has regained interest in recent years, in relation to nuclear or steel industry. In particular, predictions of heat transfer and of the flow physics during the quenching and cooling of large piece of metal is of significant interest in regards to both industrial applications and scientific issues. Since Nukiyama (1966) highlighted the different boiling regimes, the study of heat transfer during film boiling process has been the topic of several decades of research. The heat transfer has first been studied in a liquid at saturation temperature, in particularly by Bromley (1950); Bromley, LeRoy, and Robbers (1953), who analyzed film boiling around horizontal cylinder with and without forced flow. Later, Berenson (1961) investigated the influence of the Taylor-Helmholtz instability on the heat transfer during film boiling on a horizontal plate. Klimenko (1981) completed this model by taking into account turbulent vapor in the film. These early models focused only on the vapor boundary layer. The liquid boundary layer was first taken into account by Cess and Sparrow (1961a,b). They proposed a correlation for heat transfer for subcooled forced convection film boiling around a flate plate. Epstein and Hauser (1980) carried out similar studies for horizontal cylinders and spheres. Dhir and Purohit (1978) carried out experiments both on natural and forced convection film boiling around spheres in subcooled liquid and deduced a heat transfer correlation for natural and forced convection. For the natural convection this correlation is based on the separation of three contributions : the boiling heat transfer at saturation, the radiation effect, and the additional effect of natural convection in the liquid. Later, Sakurai, Shiotsu, and Hata (1990) carried out the analysis for subcooled natural convection film boiling for horizontal cylinders, and Shiotsu and Hama (2000) for subcooled natural and forced convection film boiling around vertical cylinders. In parallel with these studies, progresses in computational fluid dynamic for modelling two-phase flows with phase change were performed and have improved simulation capabilities to undertake numerical studies in such configurations. Son and Dhir (1997) were the first to simulate film boiling around a flate plate in a saturated liquid using a moving mesh to track the liquid/vapor interface and a volumetric source for the surface tension. Shortly afterward, in Son and Dhir (1998), the authors proposed further developments to capture implicitly large deformation and topology changes of the liquid/vapor interface by using the Level Set (LS) method, based on the pioneering works of Osher and Sethian (1988) and Sussman, Smereka, and Osher (1994). Others works byJuric and Tryggvason (1998) and Welch and Rachidi (2002) used respectively the Front-Tracking (FT) and Volume Of Fluid (VOF) methods to simulate film boiling around horizontal plate in a saturated liquid. Concomitantly to the Level Set method, the Ghost Fluid Method (GFM), developed by Fedkiw, Aslam, Merriman, and Osher (1999), has emerged as a Sharp Interface Method (SIM) able to account for jump conditions at the interface without artificial smoothing. Gibou, Chen, Nguyen, and Banerjee (2007) proposed a general algorithm based on the GFM to carry out boiling simulations, in particular for film boiling. Son and Dhir (2007) also used a Level Set/Ghost Fluid Method to model film boiling around horizontal cylinders in saturated liquids. To model the cylinder they defined a viscosity jump to force the no-slip condition at the boundary of the solid. 2D and 3D simulations in such configurations are presented by Son and Dhir (2008). Singh and Premachandran (2018) chose the formalism of the CLSVOF (Coupled Level Set - Volume Of Fluid) method

ORCID(s):

to simulate film boiling around horizontal cylinders, and explicitly fixed the no-slip condition. All these simulations were performed with a liquid at saturation temperature under the assumption of incompressible flows both for the liquid and vapor phases. However, unlike nucleate boiling which is related to moderate wall superheat, film boiling involves strong temperature variations in the vapor phase on small typical scales due to the large gap between the superheated wall and the saturation temperature at the interface. This implies strong density gradients inside the vapor film. As these variations are commonly neglected, we propose in this paper an original numerical approach to investigate on film boiling in a subcooled liquid around an immersed boundary under high superheated conditions, while taking into account the density variations in the vapor phase. Our numerical approach is a Level Set-Ghost Fluid method based on the principle proposed by Gibou et al. (2007) to solve the liquid-vapor phase change. It has been further validated in Tanguy, Sagan, Lalanne, Couderc, and Colin (2014) with a theoretical solution and in Huber, Tanguy, Sagan, and Colin (2017) with experimental data. This numerical solver has also been used by Urbano, Tanguy, and Colin (2019) for numerical simulations of nucleate boiling in zero-gravity conditions and of droplet condensation or vaporization in Orazzo and Tanguy (2019) and Alis, Tanguy, Kentheswaran, Rouzaud, and Estivalezes (2023), respectively. However, as most of the previous works consider low temperature variations, they do not account for density variations inside the vapor phase. In a recent paper, Mialhe, Tanguy, Tranier, Popescu, and Legendre (2023) proposed an extended model for droplet vaporization accounting for thermo-physical variations of several properties and demonstrated the significant effect of the density variations in the vapor phase on the Nusselt number of a droplet vaporizing in a superheated vapor. In particular, it is shown that higher density variations around the droplet tend to increase the Nusselt number. To account for density variations in the vapor phase, the variable density low Mach number solver developed is similar to the ones proposed by Pember, Howell, Bell, Colella, Crutchfield, Fiveland, and Jessee (1998) or Daru, Le Quéré, Duluc, and Le Maître (2010). In the present paper, a similar low Mach number variable density solver is proposed and coupled with an Immersed Boundary Method (IBM) proposed by Ng, Min, and Gibou (2009) for an incompressible solver. The coupling between these two solvers is validated in a first step on a simple configuration of free-convection around a heated horizontal cylinder. Subsequently, we proceed to a validation of the film boiling solver designed for incompressible vapor by comparing its results with analytical correlations relevant for natural convection film boiling in a saturated liquid around a horizontal cylinder. This comparative analysis demonstrates the accuracy and reliability of the proposed computational framework. Building upon these preliminary validations, we conduct a parametric study focused on subcooled natural convection film boiling around a sphere. This study leverages the variable density solver for the vapor phase and enables studying the intricate equilibrium between evaporation and condensation that leads to the stabilization of the vapor film under such challenging conditions. Additionally, our investigation delves into the characterization of both global and local heat transfer coefficient. Fully-resolved numerical simulations of the vapor film around a superheated solid object offer many physical insights to enhance our understanding of film boiling around a solid obstacle. For instance, an accurate description of the shape of the vapor film can be achieved, as well as the computation of the flow field and heat transfer inside this vapor film. In cases involving a subcooled liquid, the subtle equilibrium between vaporisation and condensation along the interface can stabilize a bubble around the superheated solid. This phenomenon, already reported in experimental studies as in (Vakarelski, Marston, Chan, and Thoroddsen, 2011), has been captured by using fully resolved computations. Therefore, even if DNS is not yet mature enough to carry out numerical predictions in industrial applications, it can be of significant interest to enhance our physical understanding of phenomena at the micro-scale, for which experimental studies can hardly provide accurate data. All this information can have a practical interest in terms of development of integrated models for computations at larger scales that cannot be achieved with DNS.

The numerical framework will be detailed in section 2. In section 3, preliminary validations of the variable density solver coupled to an Immersed Boundary Method are reported in a configuration involving free-convection around a heated cylinder in a gas. In section 4 are described numerical simulations of film boiling around superheated solid obstacles. First, computations of film boiling around a cylinder in a liquid at saturation temperature are presented and compared favorably to an semi-empirical correlation on the Nusselt number. In a second time, film boiling around a superheated sphere immersed in a subcooled is considered. In this configuration, a steady state resulting from an equilibrium between vaporization and condensation can be reached. After carrying out a parametric study based on the two Jakob numbers that characterize the system, a thorough analysis of the flow and of the heat transfer in the vapor film at steady state is presented.

2. Computational method

The formalism and the numerical methods developed for the sake of this study are detailed in this section. In a first time, the incompressible solver is briefly discussed, since it is used in a preliminary validation of film boiling around a cylinder in a saturated liquid. Next, in a second section, the low Mach number variable density solver developed for the vapor phase is presented. In a third section, we remind the jump conditions across a liquid-vapor interface on which phase change occurs. Then, Immersed Boundary conditions that must be imposed at a solid frontier are detailed for both an incompressible solver and a low Mach number

variable density solver. Finally a brief summary of numerical methods used for the sake of this study is given.

2.1. Incompressible formulation

Our initial approach was based on a incompressible two-phase flow solver accounting for boiling phenomenon at the liquid-vapor interface in an isobaric environment at an external pressure P_∞, with $P_\infty = P_{atm} = 1.01325$ bar at ambient conditions. As previously stated, many anterior works are based on an incompressible assumption for both phases which is reasonably accurate if low temperature variations are considered in the vapor phase, as for nucleate boiling. However, this assumption may become limiting in configurations involving large temperature variations in the vapor phase, as film boiling for instance. Anyway, as the incompressible solver was the starting point of this work, fundamental equations on which it is based are briefly reminded here. The governing equations, to impose respectively the conservation of mass, momentum and energy, are as follows:

$$\nabla \cdot \boldsymbol{u} = 0, \tag{1}$$

$$\rho\left(\frac{\partial \boldsymbol{u}}{\partial t} + \boldsymbol{u}\cdot\nabla\boldsymbol{u}\right) = -\nabla p + \nabla\cdot\left(2\mu\underline{\underline{\boldsymbol{D}}}\right) + \rho\boldsymbol{g}, \tag{2}$$

$$\rho C_p\left(\frac{\partial T}{\partial t} + \boldsymbol{u}\cdot\nabla T\right) = \nabla\cdot(k\nabla T). \tag{3}$$

Here, $\boldsymbol{u}$ represents the velocity vector, T the temperature, p the pressure, $\underline{\underline{\boldsymbol{D}}} = \dfrac{\nabla\boldsymbol{u} + \nabla\boldsymbol{u}^T}{2}$ represents the deformation tensor, ρ is the density, μ the viscosity, C_p stands for specific heat at constant pressure, k is the thermal conductivity, $\boldsymbol{g}$ denotes the gravity acceleration vector. Thermo-physical properties are assumed to be constant in both the liquid and vapor phases. The properties of the liquid are defined at atmospheric pressure and temperature at the infinity, T_∞, while the vapor properties are characterized at $(T_{sat}+T_w)/2$, where T_{sat} is the saturation temperature of the liquid for the considered external pressure P_∞ and T_w is the solid wall temperature. The contribution to the heat production due to viscous dissipation is neglected. Radiation effects are also neglected since the radiation local heat flux could be estimated as $q_{rad} \sim \sigma\left(T_w^4 - T_{sat}^4\right) \sim 10^5$ W.m^{-2} (with σ the Stefan-Boltzmann constant), if we consider an emissivity of 1 and a slab radiative surface, whereas the following approximation of the conduction local heat flux, $q_{cond} \sim \dfrac{k_v(T_w - T_{sat})}{\delta}$ (with k_v the vapor thermal conductivity and δ the film thickness), provides $q_{cond} \sim 10^6$ W.m^{-2} for a 100 microns thick vapor film. These orders of magnitude are comparable with existing values in the literature on film boiling Bromley (1950); Sakurai et al. (1990).

2.2. Variable density low Mach number solver

We propose in this subsection a further elaborated model to account for density variations in the vapor film. It is a based on a variable density low Mach number model, similar to the one presented in Pember et al. (1998), Daru et al. (2010) or Mialhe et al. (2023) . Pressure in the system is decomposed into two components: a thermodynamic pressure that remains uniform throughout space and a hydrodynamic pressure which can vary both with time and space, such as,

$$p(\vec{x},t) \simeq P(t) + \tilde{p}(\vec{x},t), \tag{4}$$

with $\vec{x}$ the position vector and t the time. Whereas, we will restrict our analysis in this paper to isobaric configurations, it is worth mentioning that this model can account for temporal variations of the thermodynamic pressure. The ideal gas equation of state is employed in the vapor,

$$\rho(\vec{x},t) = \frac{P(t)}{r\,T(\vec{x},t)}, \tag{5}$$

with $r = R/M$, R the ideal gas constant and M the molar mass of the vapor. This equation of state is based on the global thermodynamic pressure $P(t)$ which will be considered in this work as a constant, such as $P(t) = P_\infty$, since we only consider isobaric configurations. As a result, the mass conservation equation,

$$\nabla\cdot\boldsymbol{u} = -\frac{1}{\rho}\frac{D\rho}{Dt}, \tag{6}$$

with $\dfrac{D}{Dt}$ the total derivative, can be expressed as follows in the vapor,

$$\nabla\cdot\boldsymbol{u} = \frac{1}{T}\frac{DT}{Dt}. \tag{7}$$

As a consequence of the pressure splitting which neglects spatial variations of the pressure in Eq. (5), this model does not allow to solve propagation of acoustical waves or compressibility effects related to high speed flows, unlike compressible solvers for two-phase flows as proposed by Jemison, Sussman, and Arienti (2014), Fuster and Popinet (2018) or Urbano, Bibal, and Tanguy (2022). However, it takes into account density variations related to thermal effects, as for example thermal expansion for a heated vapor, which is of interest in the framework of film boiling. As density variations are considered only in the vapor phase, the liquid density is constant and uniform, and the zero-divergence equation is still imposed in the liquid, such as,

$$\nabla\cdot\boldsymbol{u} = \begin{cases} \nabla\cdot\boldsymbol{u_v} = \dfrac{1}{T}\dfrac{DT}{Dt}, \\ \nabla\cdot\boldsymbol{u_\ell} = 0. \end{cases} \tag{8}$$

where subscripts v and l refers respectively to the vapor and liquid phases. The momentum and energy conservation

equations, are modified accordingly to take into account the non-zero divergence in the vapor phase,

$$\rho\left(\frac{\partial \boldsymbol{u}}{\partial t}+\boldsymbol{u}\cdot\nabla\boldsymbol{u}\right)= -\nabla\tilde{p}+\nabla\cdot\left(2\mu\underline{\underline{\boldsymbol{D}}}\right)+\nabla\cdot(\lambda\nabla\cdot\boldsymbol{u}\underline{\underline{I}})+\rho\boldsymbol{g}, \tag{9}$$

$$\rho c_v\left(\frac{\partial T}{\partial t}+\boldsymbol{u}\cdot\nabla T\right)=-P_\infty\nabla\cdot\boldsymbol{u}+\nabla\cdot(k\nabla T)\,. \tag{10}$$

In these equations, λ denotes the first Lamé coefficient (which is $-2/3\mu$ in this context), $\underline{\underline{I}}$ stands for the matrix identity, and C_v is the isochoric specific heat. It is noteworthy that variable density acts in each conservation equation, but the most significant contribution is expected in the mass conservation equation, where this can model flow dilatation or contraction related to local temperature variations.

2.3. Jump condition across the liquid-vapor interface

At the vapor-liquid interface, the following jump relations are imposed across the interface to maintain, respectively, mass, momentum and energy conservation,

$$[\![\boldsymbol{u}]\!]=\dot{m}\left[\!\left[\frac{1}{\rho}\right]\!\right]\boldsymbol{n}_\Gamma, \tag{11}$$

$$[\![p]\!]=\gamma\kappa+\left[\!\left[2\mu\boldsymbol{n}_\Gamma\cdot\underline{\underline{\boldsymbol{D}}}\cdot\boldsymbol{n}_\Gamma\right]\!\right] +[\![\lambda\boldsymbol{n}_\Gamma\cdot\left(\nabla\cdot\boldsymbol{u}\underline{\underline{I}}\right)\cdot\boldsymbol{n}_\Gamma]\!]-\dot{m}^2\left[\!\left[\frac{1}{\rho}\right]\!\right], \tag{12}$$

$$[\![-k\nabla T\cdot\boldsymbol{n}_\Gamma]\!]=\dot{m}\,h_{\ell\to v}. \tag{13}$$

In these equations, $[\![A]\!]$ is defined as the jump operator at the interface, $[\![A]\!]=A_\Gamma^+-A_\Gamma^-$, where Γ refers to the interface, A_Γ^+ represents the value of the variable A at the interface in phase +, and vice versa for A_Γ^-. Additional parameters include the surface tension γ, the interface curvature κ, the latent heat $h_{\ell\to v}$, and the local vaporization rate $\dot{m}$, which is defined as $\dot{m}=\rho^-(\boldsymbol{u}^--\boldsymbol{u}_\Gamma)\cdot\boldsymbol{n}_\Gamma=\rho^+(\boldsymbol{u}^+-\boldsymbol{u}_\Gamma)\cdot\boldsymbol{n}_\Gamma$. The normal vector at the interface pointing towards the vapor phase is denoted as $\boldsymbol{n}_\Gamma$, and $\dfrac{\partial u_n}{\partial n}$ represents the derivative of the normal component of velocity with respect to the normal direction at the interface. These jump conditions are valid whether an incompressible or a variable-density formalim is used. The only difference lies on the third term of the right hand side of Eq. (12) which is zero on each side of the interface if an incompressible solver is used in the two phases, whereas it has a non-zero value in the vapor in case of a the variable density solver. Finally, a last condition is imposed on the temperature of the liquid-vapor interface, which is assumed to be equal to the saturation temperature,

$$T_\Gamma=T_{sat}. \tag{14}$$

This assumption relies upon the assumption of local thermodynamical equilibrium at the liquid-vapor interface.

2.4. Immersed boundary condition at the solid frontier

In this section, the boundary conditions that must be applied at the solid-vapor interface Γ_w are described. It is worth mentioning that, in this paper, investigations are restricted solely to vapor film around solid obstacles, and do not consider further contact angles and related capillary effects at a contact line since such phenomena, characteristic of nucleate boiling, do not appear in the case of film boiling. A schematic of a typical configuration of interest is presented in Fig. 1.

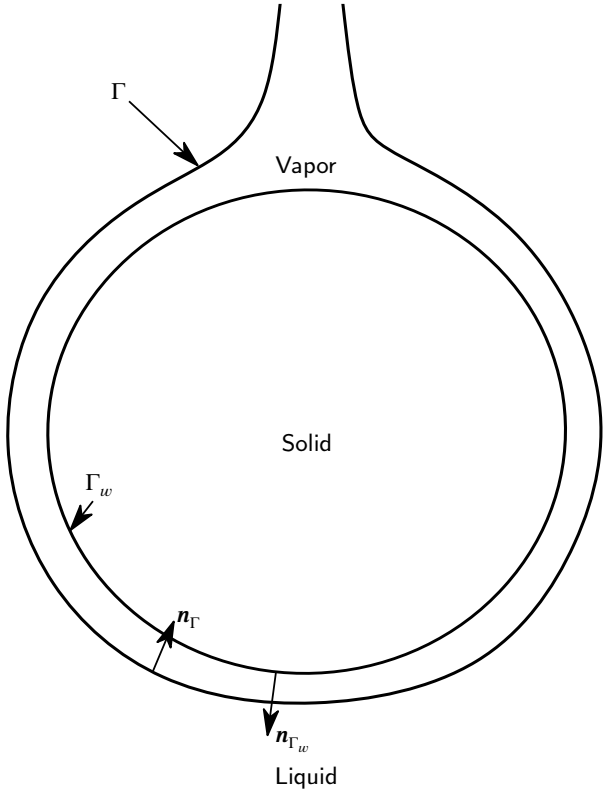

Figure 1: Scheme of film boiling around a horizontal cylinder or a 2D sphere with the interfaces and there normal vectors.

Regarding the solid interface immersed in a fluid, we apply classical boundary conditions for pressure and the velocity components at the solid frontier, that is, an impermeability condition which is consistent with a zero pressure gradient along the normal direction at the interface,

$$\boldsymbol{n}_{\Gamma_w}\cdot\nabla P|_{\Gamma_w}=0, \tag{15}$$

and a zero normal velocity,

$$\boldsymbol{n}_{\Gamma_w} \cdot \boldsymbol{u}|_{\Gamma_w} = 0, \tag{16}$$

where $\boldsymbol{n}_{\Gamma_w}$ is the normal vector at the solid frontier Γ_w. For a viscous fluid, a no-slip condition has also to be imposed on the solid frontier which can be written as,

$$\boldsymbol{t}_{\Gamma_w} \cdot \boldsymbol{u}|_{\Gamma_w} = 0, \tag{17}$$

where $\boldsymbol{t}_{\Gamma_w}$ is the tangent vector at the solid frontier. Regarding the thermal boundary condition on the immersed solid obstacle, an uniform and constant temperature T_w is applied, such as,

$$T_{\Gamma_w} = T_w, \tag{18}$$

which means that only isothermal solid obstacles are considered in this study. An extended model accounting for conjugate heat transfer between the solid and fluid domains should be based on the local heat flux continuity, instead. Such a coupling would enable to compute temperature variations in the solid in relation with the heat flux exchanged at the solid-fluid interface. However, as the scope of this paper is essentially to investigate on the local film structure at steady state, such unsteady effects are not considered in this study and an uniform Dirichlet boundary condition on the temperature is imposed on the solid frontier.

2.5. Numerical methods

The numerical computations in this study are conducted using the in-house code, DIVA, which is based on the Level Set method for capturing liquid-vapor interfaces, as proposed by Osher and Sethian (1988) and Sussman et al. (1994). For computing convective terms, the fifth-order Weno-Z scheme, proposed by Borges, Carmona, Costa, and Don (2008), is implemented, while diffusion terms are discretized with classical second-order finite volume schemes. Our two-phase flow solver falls within the category of Sharp Interface Methods (SIM), and avoids any artificial smoothing of the source term at the interface. Jump conditions are imposed following the guidelines of the Ghost Fluid Method of Fedkiw, Marquina, and Merriman (1999). In particular, the boiling solver is similar to the one proposed by Gibou, Chen, Nguyen, and Banerjee (2007), which is also refered as the Ghost Fluid Thermal Solver for Boiling (GFTSB) in Rueda Villegas, Alis, Lepilliez, and Tanguy (2016). Immersed Dirichlet boundary conditions at the interface are imposed with the second order scheme proposed by Gibou, Fedkiw, Cheng, and Kang (2002), both for T_{sat} at the liquid-vapor interface and T_w at the solid frontier. The jump condition on the normal velocity at the interface is computed with the numerical method proposed by Nguyen, Fedkiw, and Kang (2001). An another important feature of GFTSB is to compute the phase change mass flow rate $\dot{m}$ with the jump condition related to the energy conservation equation Eq. (13), such as,

$$\dot{m} = \frac{[\![-k\nabla T \cdot \boldsymbol{n}_{\boldsymbol{\Gamma}}]\!]}{h_{\ell \to v}}, \tag{19}$$

in which a vapor or a liquid heated above or cooled below the saturation temperature will induce vaporization or condensation, respectively. In Tanguy et al. (2014), it is shown that the accuracy can be enhanced by implementing a second-order extrapolation for the temperature fields, as described in Aslam (2004). The solid boundary condition at the solid frontier are imposed with the sharp Immersed Boundary Method (IBM) proposed by Ng, Min, and Gibou (2009) and further extended to two-phase flows by Lepilliez, Popescu, Gibou, and Tanguy (2016). In particular, it is based on a second order method for imposing the pressure Neumann boundary condition at the solid frontier, Eq. (15), and it also uses the second order numerical scheme proposed by Gibou et al. (2002) for immersed Dirichlet boundary conditions on velocity components given by Eq. (16) and Eq. (17). A subcell resolution is used to maintain second order accuracy at the interface, which implies an implicit temporal discretization of the viscous terms, as detailed in Lepilliez et al. (2016) for isothermal two-phase flows with an IBM. As the linear system, resulting from the coupling between all the velocity components, is diagonally dominant, it can be solved efficiently with a simple Gauss-Seidel method. The linear system resulting from the pressure Poisson equation, which is typical of incompressible and low Mach number variable density solvers, is efficiently solved using a Black-Box MultiGrid method proposed by Dendy (1982). In particular, it enables a fast resolution of the pressure Poisson equation even in configurations with strong density ratio between the liquid and vapor phases. Overall temporal integration is performed using a second-order Runge-Kutta scheme. Full details on the implementation of the low Mach number variable density solver can be found in the following reference, Mialhe et al. (2023). It is a pressure based solver very similar to an incompressible projection method, whereas some additional source terms have to be added in equations to account for local density variations. In particular, the non-zero divergence term which accounts for flow expansion or contraction appears as as source term in the Poisson equation.

3. Validations of the variable density solver with an IBM in a free-convection configuration

The overall solver briefly detailed in the previous section has been extensively validated with many experimental data in the framework of nucleate boiling in Huber et al. (2017) and Torres, Urbano, Colin, and Tanguy (2024), of Leidenfrost Droplets in Rueda Villegas, Tanguy, Castanet, Caballina, and Lemoine (2017) and Mialhe et al. (2023) or for the dynamics of bubbles contaminated by surfactants in Kentheswaran, Dietrich, Tanguy, and Lalanne (2022). The IBM solver adapted to isothermal two-phase flows has also

been accurately validated with experiments in micro-gravity conditions in Dalmon, Lepilliez, Tanguy, Pedrono, Busset, Bavestrello, and Mignot (2018) and Dalmon, Lepilliez, Tanguy, Alis, Popescu, Roumiguié, Miquel, Busset, Bavestrello, and Mignot (2019). However, before undertaking more complex simulations involving film boiling around an IBM, for the sake of this study, additional validations of the variable density low Mach Number solver coupled to an IBM are required. In particular, a preliminary test-case is presented in this section for a single phase flow. It consists in a free-convection flow around a hot horizontal cylinder.

3.1. Computational domain and initial conditions for convection in air

To evaluate the implementation of the variable density solver coupled to an IBM, a study of air convection around a horizontal heated cylinder is proposed and compared to experimental and numerical results presented by Atayılmaz and Teke (2009). The initial conditions for each simulation are defined and summarized in Table 1 in which Ra is the Rayleigh number defined as,

$$Ra = \frac{g\,(T_w - T_\infty)\,D^3}{T_\infty\,\nu\,\alpha} \tag{20}$$

for an ideal gas with ν, the cinematic viscosity and α the thermal diffusivity. Air properties, crucial for our simulations, come from the CoolProp database[1], which relies on data from Lemmon, Jacobsen, Penoncello, and Friend (2000) and Lemmon and Jacobsen (2004).

Our computational domain measures $20D$ in width and $30D$ in length, with D representing the diameter of the cylinder. This large size domain is required to avoid boundary effects which can be critical in free convection configurations. The center of the cylinder is located $10D$ above the bottom of the domain. This configuration aligns with established practices in the field, as corroborated by prior studies (Kuehn and Goldstein (1980); Ma and He (2021)). As illustrated in Fig. 2, the boundary conditions imposed at the frontier of the domain are the following: periodic boundary conditions are enforced on the lateral sides of the domain, an outflow and a zero-heat flux boundary conditions are respectively applied on the velocity and the temperature on the upper part of the domain. These boundary conditions closely align with those utilized by Heo et al. (Heo, Chae, and Chung (2013)) and Sebastian et al. (Sebastian and Shine (2015)). A no-slip boundary condition is set on the bottom of the domain and a Dirichlet boundary condition for the temperature field. As a large domain size is computed, the influence of the bottom boundary condition on the results has been verified to be negligible on the overall solution.

3.2. Mesh requirement

To determine the appropriate mesh refinement necessary to accurately capture coupled hydrodynamic and thermal effects, a mesh sensitivity analysis was conducted, with a specific focus on Case 1 (see Table 1), characterized by the highest Rayleigh number, and therefore the most stringent condition on the cell size. Four possible meshes have been tested, which are 512×1024, 1024×2048, 2048×4096 and the most refined grid 4096×8192. To demonstrate the ability of the numerical solver to compute coupled heat transfer and local aerodynamics, the Nusselt number of the solid cylinder has been calculated in each configuration with the following expression,

$$Nu = \frac{\frac{1}{S_{cyl}} \oiint_{\Gamma_w} -k_v \nabla T \cdot \boldsymbol{n}_{\boldsymbol{\Gamma_w}} dS}{k_v (T_w - T_\infty)/D} \tag{21}$$

where ∇T is the local thermal gradient at the solid/vapor interface, D is the cylinder diameter, and S_{cyl} is the surface of the cylinder. As depicted in Fig. 3, the temporal evolution of the Nusselt number shows that a stabilized value is reached until a time integration of approximately $t \sim 1.0$ s.

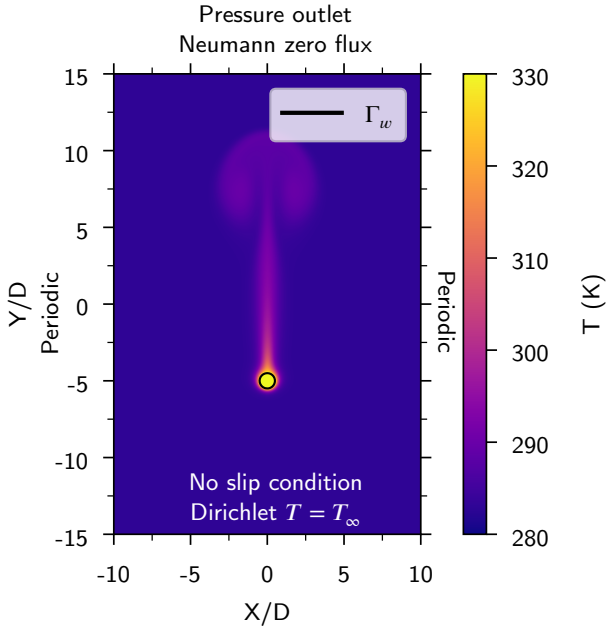

Figure 2: Thermal field, computational domain and boundary conditions for air convection around a horizontal cylinder at t = 2.0409 s.

Table 1
Initial conditions for air convection simulation.

Case	T_w (K)	T_∞ (K)	D (mm)	Ra
1	333.65	282.96	9.45	3514.07
2	323.16	313.44	9.45	51.92
3	333.24	313.42	9.45	1104.23
4	303.30	293.41	9.45	797.54
5	323.44	293.30	9.45	2087.42
6	333.51	293.38	9.45	2578.26
7	313.53	293.40	9.45	1501.01
8	293.83	284.39	4.8	115.38

[1] http://www.coolprop.org/

It also demonstrates the convergence of the solution when increasing the grid resolution. As there is no theoretical solution of this problem, the simulation result obtained with the most refined grid is defined as reference solution in order to analyze the error and the convergence order. The results of the grid sensitivity on the Nusselt numbers are compiled for Case 1 in Table 2. This indicates errors on the cylinder Nusselt number ranging between 10.89% to 1.95% from the coarsest grid 512 × 1024 to the intermediate grid 2048 × 4096, with a 1.2 convergence order, approximately.

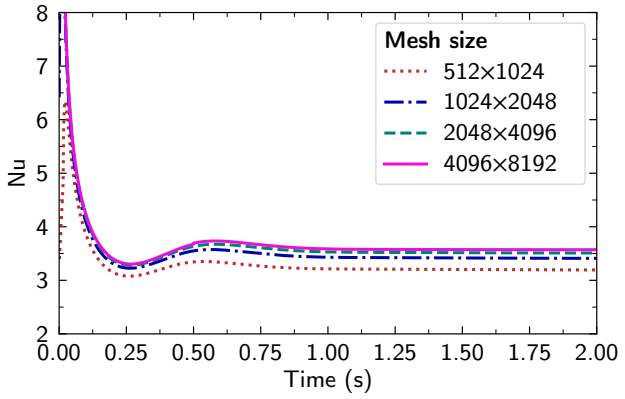

Figure 3: Nusselt number as a function of time for air natural convection case 1 with different mesh refinement.

The thermal field in the whole computational domain is presented in Fig. 2 at the final time of the simulation, $t = 2.0409$ s. A closer view of the streamlines and of the thermal field in the vicinity of the cylinder is plotted in Fig. 4 to illustrate the free convection flow that develops around the cylinder. A boundary layer is observed around the cylinder, but without flow separation.

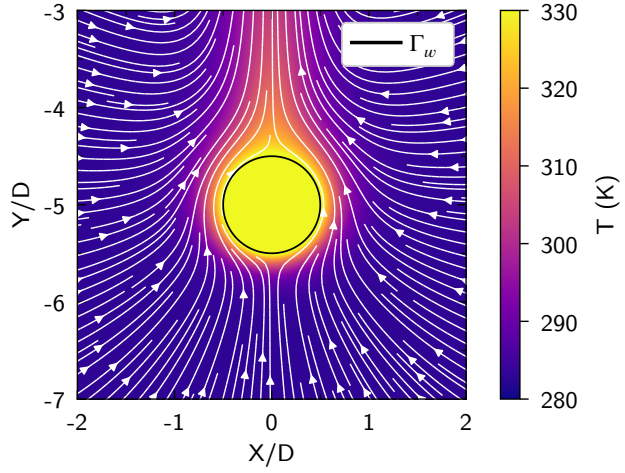

Figure 4: Thermal field and streamlines for air convection around a horizontal cylinder at t = 2.0409 s.

The velocity field has also been plotted in Fig. 5 with the mesh resolution 2048 × 4096 to visualize the upward flow induced by buoyancy effect and the boundary layer forming around the cylinder. As the grid resolution 2048 × 4096 provides relevant results in this case, it was employed for the other simulations presented hereinafter.

Table 2
Convergence on Nusselt number for the case 1. Error are relative to the 4096 × 8192 mesh size case.

Mesh size	Nu	Error (%)	Order
512 × 1024	3.19	10.89	/
1024 × 2048	3.41	4.75	1.20
2048 × 4096	3.51	1.95	1.20
4096 × 8192	3.58	reference solution	/

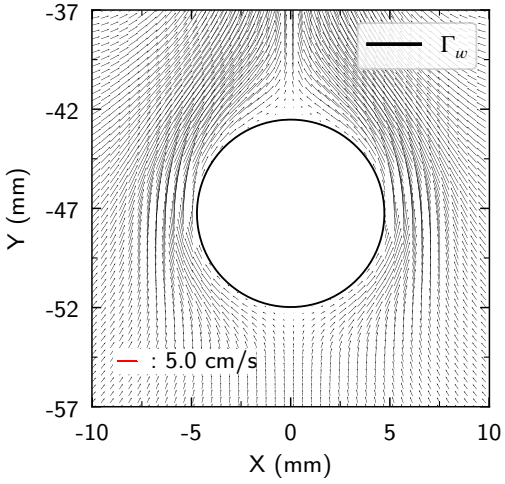

Figure 5: Velocity vector field at 2.0409 s for air convection around a horizontal cylinder. For better readability only one over 5 vector is represented.

3.3. Parametric study

For the sake of validations of the variable density solver coupled to IBM, a parametric study has been carried out considering various parameters as outlined in Table 1. Global Nusselt number computed in our simulations are superimposed with experimental and numerical results of Atayılmaz and Teke (2009) in Fig. 6. It is noteworthy that the numerical results, obtained by Atayilmaz et al, were obtained from a 2D simulation with the commercial CFD software Fluent. Although their simulation involved an exceptionally large computational domain, our smaller domain still captures the trend and aligns closely with both the numerical and experimental results presented in Fig. 6.

The comparison between our simulation results and the correlation found in Atayılmaz and Teke (2009) demonstrates a reasonably good agreement, falling within a range of approximately ±15%, as it is also the case if the correlation is compared to the experimental data.

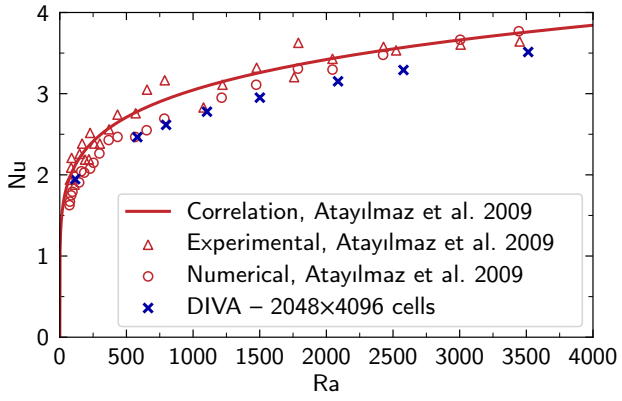

Figure 6: Global Nusselt number as a function of Rayleigh number for air convection around a horizontal cylinder.

Table 3
Liquid and vapor properties for the simulation around a horizontal cylinder in a saturated liquid

Properties	Liquid	Vapor
k, thermal conductivity (W/m/K)	0.677	0.0245
ρ, density (kg/m^3)	300	0.590
C_p, heat capacity (J/kg/K)	4.22×10^3	2.08×10^3
μ, dynamic viscosity (Pa.s)	2.82×10^{-4}	1.22×10^{-5}
Pr (Prandtl number)	1.76	1.03
Boiling and two phase flow properties		
Wall Superheat (K)	200	
$h_{\ell \to v}$, latent heat (J/kg)	2.26×10^6	
γ, superficial tension (N/m)	0.0589	
T_{sat}, saturation temperature (K)	373	
Ja (Jakob number)	0.184	

4. Validations, numerical results and discussion on film boiling configurations

In this section, numerical investigations on film boiling around solid objects are now presented. Although, this study is essentially focused on film boiling around a sphere, a benchmark involving film boiling around a horizontal heated cylinder immersed in water at saturation temperature is proposed in a first time for the sake of validation of the film boiling solver. Numerical results are then compared to an existing semi-empirical correlation, since such correlations do not exist for a superheated sphere in a subcooled liquid. In a second part, original results of film boiling around a sphere in a subcooled liquid are reported for different superheated Jakob numbers. A stable film shape, resulting from the equilibrium between vaporization and condensation, can be reached in such configurations. This allows to perform an accurate analysis on the local and global Nusselt numbers at steady state, as well as detailed investigations on the flow field in the vapor film and on the equilibrium between vaporization and condensation.

4.1. Film boiling in saturated liquid around a horizontal cylinder

A direct comparison between our numerical solver and existing semi-empirical correlations proposed by Bromley (1950); Sakurai et al. (1990) is now presented in the configuration of film boiling around a horizontal cylinder. As these analytical studies assume an incompressible flow in the vapor film, we also consider a constant density in our simulations. In both theoretical models, the authors neglected convection effect in the vapor film, assuming solely conduction and radiation heat transfer. As the latter is not considered in our overall model, the Nusselt extracted from our numerical simulations is compared to the following expressions that also neglect radiation,

$$Nu = 0.62 \left[\frac{\rho_v(\rho_\ell - \rho_v) g h'_{\ell \to v} D^3}{k_v \Delta T_{sup} \mu_v} \right]^{0.25}, \tag{22}$$

where $h'_{\ell \to v} = h_{\ell \to v} \left(1 + 0.4 \frac{c_{p_v} \Delta T_{sup}}{h_{\ell \to v}} \right)$ and,

$$Nu = 0.612 M^{1/4}, \tag{23}$$

from Bromley (1950) and Sakurai et al. (1990), respectively. The expression of the coefficient M in equation (23) is described in Sakurai et al. (1990). The properties employed for the vapor and liquid phases are listed in Table 3 in which Pr is the Prandtl number,

$$Pr = \frac{\mu C_p}{k}, \tag{24}$$

Ja is the Jakob number,

$$Ja = \frac{C_{pv}(T_w - T_{sat})}{h_{\ell \to v}}. \tag{25}$$

It is noteworthy that for computational cost reasons, the liquid density has been decreased to 300 $kg.m^{-3}$ to enlarge slightly the vapor film thickness. Indeed, the larger is the density ratio, the thinner is the vapor film. Therefore, reducing the liquid density to a smaller value allows to alleviate the drastic constraint on the size of the computational cell required to describe accurately the vapor film. The diameter D of the horizontal cylinder is taken at $D = 2$ mm and at the initialization of the simulation, the film thickness was set at 0.25 mm, with a constant temperature gradient imposed within the vapor film region.

The dimensions of the computational domain are $L_x = 15$ mm and $L_y = 30$ mm. Boundary conditions and initial condition for the film initialization are illustrated in Fig. 7. Given the high density ratio, the resulting vapor film is thin compared to the dimensions of the solid, which requires thin computational cells to capture accurately the thermal and dynamical effects in the vapor film. In Fig. 8 snapshots of the temperature field and of interface profiles are plotted at different times from the simulation with a resolution 2048×4096. The initial snapshots in Fig. 8(a) and Fig. 8(b) show the bubble growth process. In Fig. 8(c),

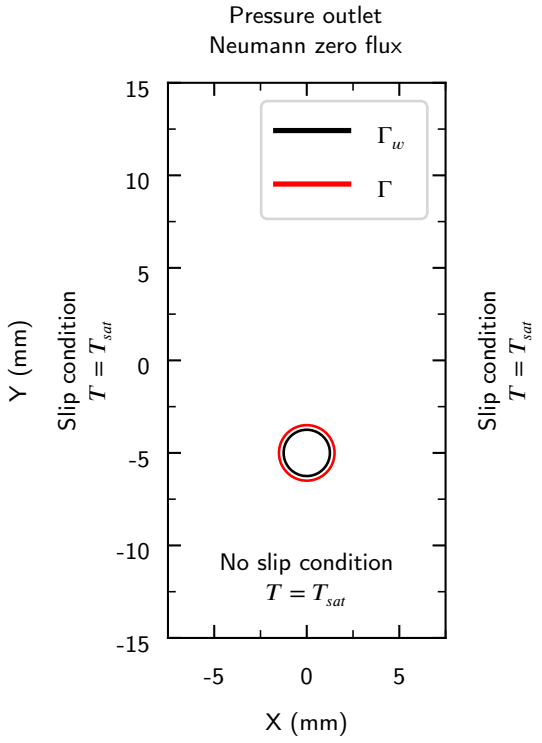

Figure 7: Simulation domain for the film boiling simulation around a horizontal cylinder in a saturated liquid.

one can observe the interface shape just before the bubble detachment. This results in a pinched vapor film between the middle and the top of the cylinder. Subsequently, the bubble detaches, and starts another bubble growth cycle, as observed in Fig. 8(d).

The Nusselt number as a function of time is depicted in Fig. 9, for different mesh refinements, that is 1024×2048, 2048×4096 and 4096×8192. Unlike correlations which are based on a steady state assumption and thus predict a static Nusselt number, our simulations exhibit unsteady behaviors related to interface oscillations from which results Nusselt oscillations at the first time of the simulations. These oscillations may result of the initial conditions on the film profile, and they are finally damped over time. Next, moderate increase of the Nusselt number is observed until the bubble detachment which occurs at $t \sim 0.25 - 0.3$ s. As the two more refined grids 2048×4096 and 4096×8192, provide results in close agreement, the grid convergence of the numerical simulation can be concluded from this mesh sensitivity study.As the simulation on the finest grid involves a significant computational cost, it was not conducted until the final time. However, the time integration is long enough to clearly observe in Fig. 9 the mesh convergence between intermediate and finest grids. Finally, if compared to the correlations from Bromley (1950); Sakurai et al. (1990), the simulations predict slightly higher values, especially at the final time before the bubble detachment occurs. However, it is noteworthy that these correlations consider a steady vapor film and no bubble detachment. Consequently, one can conclude on a relative good agreement between numerical results and the correlations from Bromley (1950). To investigate further on the flow structure in the vapor film, snapshots of the velocity field inside the film are plotted in Fig. 10 at the critical time just before the bubble detachment at $t = 0.27s$. Fig. 10(a) shows clearly the strong velocity jump at the bottom of the cylinder induced by high values of phase change mass flow rate $\dot{m}$ which strongly contributes to the vapor mass flow rate along the cylinder. In Fig. 10(b), higher velocity vapor flow of 2.15 m/s can be visualized in the pinched region that appears in the wake of the cylinder. These high velocities are related to the vapor film thinning due to the pinch. In Fig. 10(c), a characteristic parabolic velocity profile is observed at the middle of the cylinder which is induced by viscous effects inside the vapor film. Finally, in Fig. 10(d) is plotted a global view of the cylinder and of the vapor film on which are tagged the three points represented in Fig. 10(a,b,c)

To conclude this section, it is worth mentioning that the grid resolution inside the vapor film is the key parameter to describe successfully the film boiling regime. Around 5-10 computational cells inside this vapor film are required to achieve its description with a sufficient accuracy. This requirement will be observed in the computations presented in the following section dedicated to the film boiling around a sphere immersed in a subcooled liquid.

4.2. Film boiling in subcooled liquid around a sphere

After carrying out validations of the numerical solver in two configurations, that is free-convection around a horizontal heated cylinder immersed in a gas and film boiling around a superheated horizontal cylinder immersed in a saturated liquid, film boiling around a sphere in a subcooled liquid is now considered. Our long term interest is to study the effect of film boiling on heat transfer during metals hardening. However, such industrial set-ups involve large-sized metallic pieces which are currently out of reach for DNS solvers. Therefore, our study aims to provide physical insights on the flow structure and heat transfer at the vapor film scale for smaller solid objects. To this end, a 1 mm diameter sphere has been considered in this study. A parametric study is presented to investigate on film boiling in subcooled liquid around this millimetered-size sphere. This study is based on both the variable density solver for the vapor phase and the film boiling solver presented in this paper. The parametric study has focused on the variations of the Nusselt number with the two Jakob numbers that characterize the configuration, the superheated Jakob number with respect to the wall and saturation temperatures,

$$Ja_{sup} = \frac{C_{pv}(T_w - T_{sat})}{h_{\ell \to v}}, \tag{26}$$

and the subcooled Jakob number based on the saturation temperature and the subcooled liquid temperature in the far field T_∞,

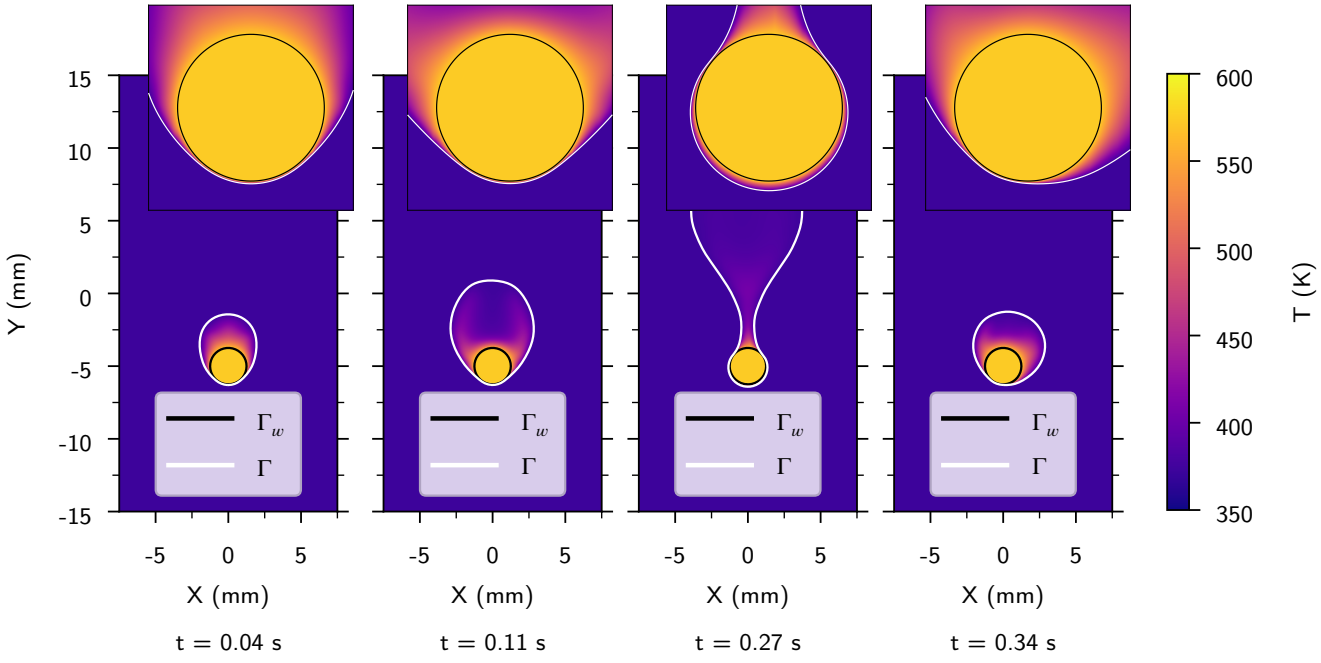

Figure 8: Temperature field at different time for film boiling simulation around an horizontal cylinder in a saturated liquid.

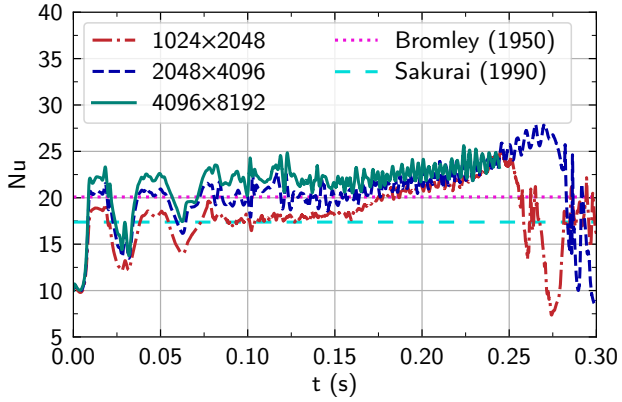

Figure 9: Nusselt number for the film boiling simulation around a horizontal cylinder in a saturated liquid for different mesh refinment.

$$Ja_{sub} = \frac{C_{pl}(T_{sat} - T_\infty)}{h_{\ell \to v}}. \tag{27}$$

Properties of the liquid and vapor phases are identical to those presented in Table 3, except for the latent heat and the Jakob numbers. The simulations presented in this section involve a high superheat case, $\Delta T_{sup} = T_w - T_{sat} = 800K$, and a low subcooling case, $\Delta T_{sub} = (T_{sat} - T_\infty) = 5K$. These conditions resulted in a superheated Jakob number Ja_{sup}, and a subcooled Jakob number Ja_{sub}, ranging from 1.51 to 5.54 and 0.019 to 0.07, respectively. Jakob numbers have been varied by means of the latent heat $h_{\ell \to v}$ with values ranging from 300 000 to 1 100 000 $J.kg^{-1}$. While lower than latent of water, this range of values is typical of most liquids. It is worth mentioning that higher values involve a lower Ja_{sup} number and thus may reduce the vapor film thickness which makes more difficult its computation. The numerical simulations are now performed in an axisymmetric coordinates system in order to simulate the flow around a sphere, instead a cylinder as it was in previous sections. The computational domain and boundary conditions are the same as described in Section 4.1, except for the Dirichlet boundary conditions on the temperature which are set at T_∞, and the left side which is the axisymmetric axis. The simulations have been performed with a grid 2048 × 4096 for which grid convergence has been reported in the previous configurations. As we consider film boiling in a subcooled liquid, there is no bubble detachment since a quasi-steady state resulting from a subtle equilibrium between vaporization and condensation can be reached, as observed in Fig. 11. The temperature fields in the vapor phase as well as the liquid-vapor interface profile are plotted in Fig. 11(a) and Fig. 11(b) for two Jakob numbers, that is $Ja_{sup} = 3.32$ and $Ja_{sup} = 1.51$, respectively. In these figures, the thin structure of the vapor film can be visualized in the bottom part of the sphere, whereas it significantly enlarges in the upper part and it forms a large vapor bubble attached around the superheated sphere. As previously stated, the bubble attachment results from an equilibrium between vaporization which prevails in the bottom part of the film whereas condensation occurs in the upper part. It is worth mentioning that experimental observations of such stabilized vapor films have already been reported by Vakarelski, Marston, Chan Derek, and Thoroddsen (2011), for larger superheated spheres. The asymmetry between the bottom and the top of the sphere is induced by the buoyancy effect which tends to move the bubble upward, from which

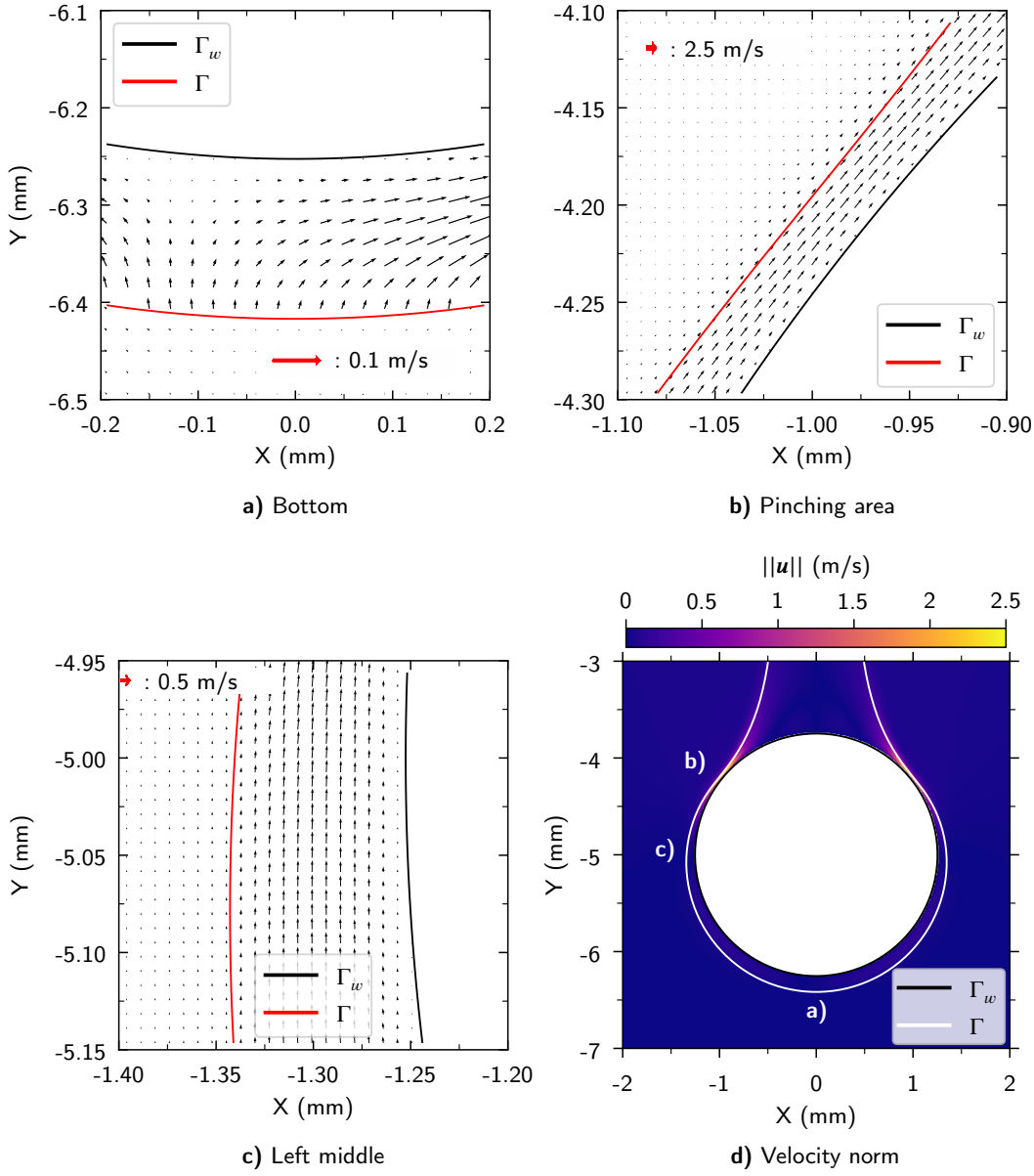

Figure 10: Velocity field at time t = 0.27 s for the film boiling simulation around an horizontal cylinder in a saturated liquid. **a)** Bottom of the cylinder, for this area only, one over four vector is represented for better readability, **b)** pinched region, **c)** middle left of the sphere, **d)** velocity norm around the cylinder. Red arrows correspond to the reference scale vectors.

results the film thinning in the lower part of the bubble. Temperature fields in the liquid are also plotted in Fig. 11(c) and Fig. 11(d) for the two previous Jakob numbers. A large thermal wake is observed at the rear of the bubble attached around the sphere. All these figures highlight the significant effect of the interface shape on the local temperature field and thus on the local Nusselt number at the solid frontier and on $\dot{m}$, the local phase change mass flow rate. To illustrate this, $\dot{m}$ is plotted in Fig. 12 in the bottom part of the sphere. This enables to visualize the transition between vaporization (positive values of $\dot{m}$) and condensation (negative values of $\dot{m}$) as the film thickness is increasing along the liquid-vapor interface. Although $\dot{m}$ is physically defined only at the interface, an extension of this variable along the normal direction is required to improve the stability and accuracy of computations. However, this extension does not alter the sharp description of the interface, since source terms and discontinuities are still located solely in the computational cells crossed by the zero-level curve of the level set function. More details on this specific point can be found in the following references Tanguy et al. (2014) and Bibal, Deferrez, Tanguy, and Urbano (2024).

Further investigations on the Nusselt number of the sphere are now presented. At steady state, the angular local Nusselt number Nu_θ is defined as,

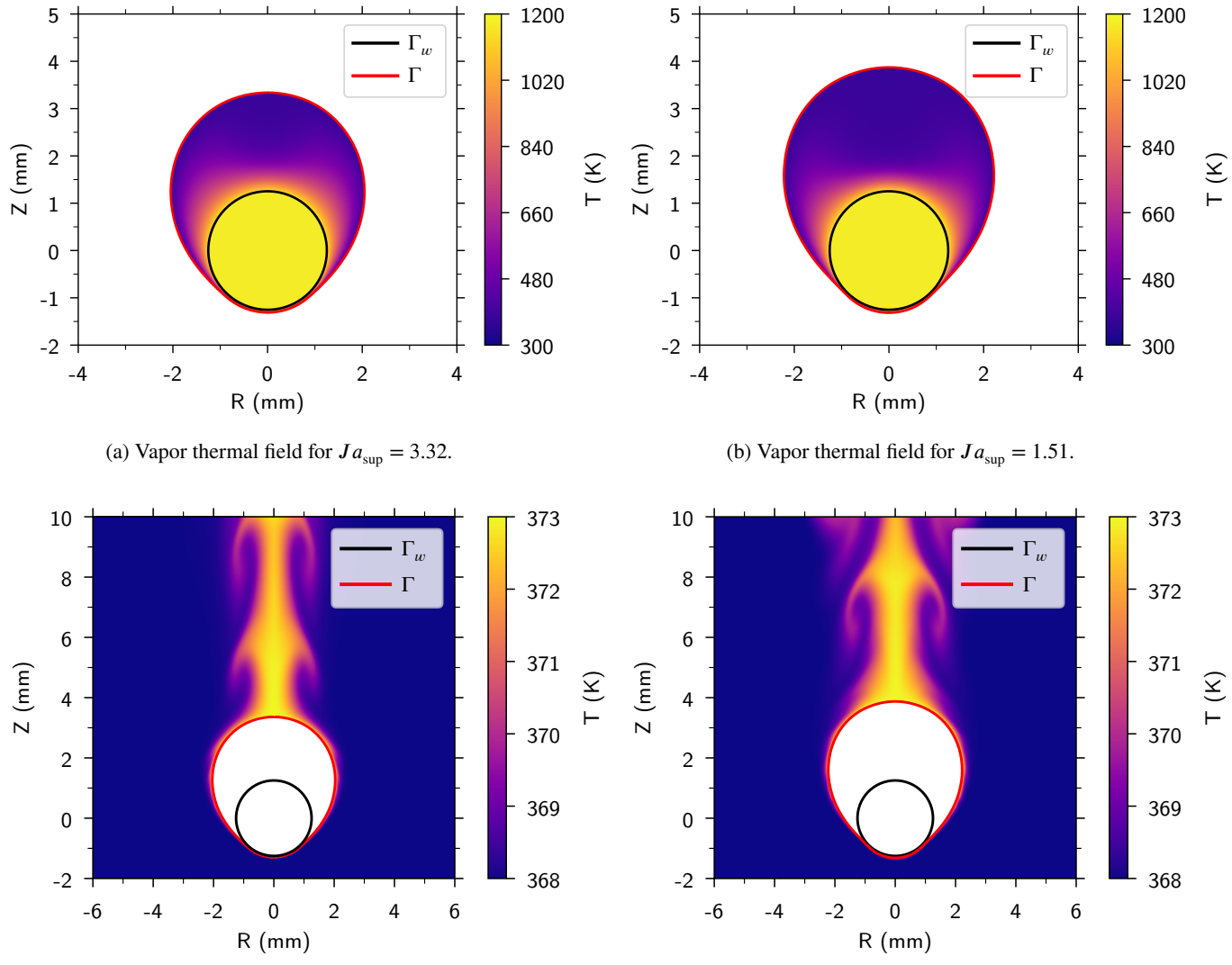

(a) Vapor thermal field for $Ja_{\text{sup}} = 3.32$.

(b) Vapor thermal field for $Ja_{\text{sup}} = 1.51$.

(c) Liquid thermal field $Ja_{\text{sup}} = 3.32$.

(d) Liquid thermal field for $Ja_{\text{sup}} = 1.51$.

Figure 11: Steady interface shape, vapor and liquid thermal field for the subcooled film boiling around spheres for $Ja_{\text{sup}} = 3.32$ at t = 0.18164 s and $Ja_{\text{sup}} = 1.51$ at steady state

$$Nu_\theta = \left.\frac{-k_v \nabla T \cdot \boldsymbol{n}_{\boldsymbol{\Gamma_w}}}{k_v (T_w - T_\infty)/D}\right|_{R,\theta \in \Gamma_w} \tag{28}$$

with θ the angle of the spherical coordinates associated to the center of the solid sphere. θ is set to 0° at the bottom of the sphere and to 180° at the top of the sphere. In Fig. 13, the angular variation of Nu_θ is plotted with full line for all the Jakob numbers of the parametric study. Many information can be extracted from these curves. First, for lower angles ranging from 0° to approximately 45°, a kind of plateau is observed with maximal values of the angular Nusselt number varying between 40 to 50 according to the value of Ja_{sup}. If compared to the reference Nusselt number of a sphere in a purely conductive problem which is equal to 2, these values correspond to high heat transfer coefficient induced by a very thin vapor film thickness. For most of the curves presented in Fig. 13 (i.e. $Ja_{sup} = 1.51, 1.85, 2.37$), a maximum value of the local Nusselt number is observed for angles around 45°. A quick decrease of the Nusselt number is seen due to the thickening of the vapor film. Finally, the local Nusselt number tends to another plateau with a much lower value, around 5, for angles between 90° to 180°. It is worth mentioning that these values of the Nusselt number in the rear of the cylinder depends weakly on Ja_{sup}. In Fig. 13, additional curves of the Nusselt number are plotted in dashed lines. These curves are based on the following estimation of the Nusselt number,

$$Nu_{\theta,c} = \frac{q_{\theta,c}}{q_{ref}}, \tag{29}$$

in which we have,

$$q_{\theta,c} = k_v \left(\frac{T_w - T_{sat}}{\delta(\theta)} \right) \text{ and } q_{ref} = k_v \left(\frac{T_w - T_{sat}}{D} \right). \tag{30}$$

$q_{\theta,c}$ is a conduction heat flux based on the local film thickness $\delta(\theta)$ defined as, $\delta(\theta) = d(\theta) - R_s$, with $d(\theta)$ the distance between the center of the droplet and the liquid-vapor interface along a given direction associated to the angle θ. q_{ref} is the reference heat flux for a conduction problem around a heated sphere in an infinite medium. Therefore, dashed line curves neglect the effect of the vapor flow in the film since it provides an estimation of the wall heat flux solely based on the heat conduction. On the other hand, full line curves, coming from DNS, fully account for convection effect in the vapor film. The interest is to compare, for a given film thickness, dashed line to full line curves in order to estimate the effect of convection in the vapor film on the local heat flux. One can observe that for most Ja_{sup}, both curves coincide in the lower part, for $0° < \theta < 90°$, whereas significant differences appear in the upper part for $90° < \theta < 180°$.

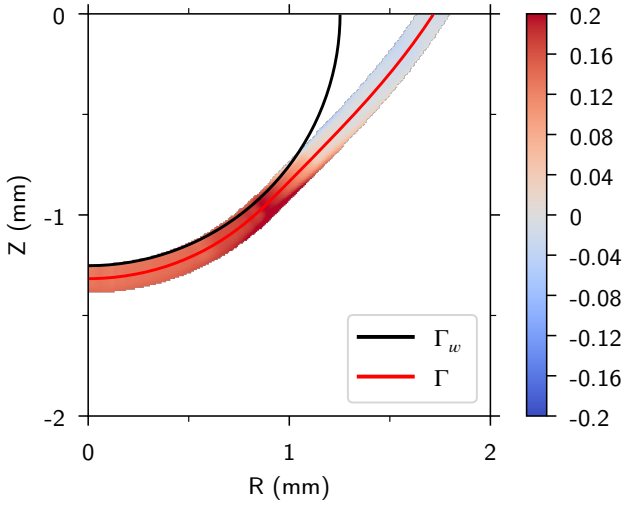

Figure 12: Local field of the vaporization/condensation mass flow rate $\dot{m}$ around the liquid/vapor interface in the bottom part of the sphere for $Ja_{sup} = 1.51$ at steady state.

This means that convection has little effect on the local thermal flux in the bottom part of the sphere where the vapor film is the thinnest and the local heat transfer is the largest, but it cannot be neglected in the upper part where the vapor film becomes much thicker. Indeed, the thicker vapor film in the upper part allows the development of additional convective cells, leading to higher values of the Nusselt number than for configurations with solely heat conduction. For the sake of illustration, such convective cells can be visualized in Fig. 14 where recirculating flow inside the vapor layer in the wake of the sphere are observed.

Regarding the simulation with the highest superheated Jakob number, $Ja_{sup} = 5.54$, it is worth mentioning that the

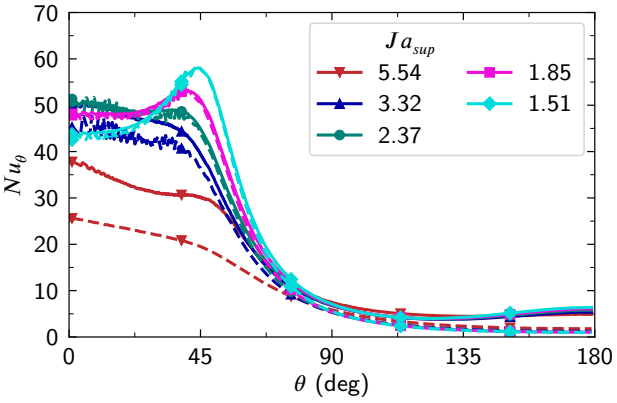

Figure 13: Angular Nusselt number Nu_θ as a function of θ. Dashed line is for the pure conductive Nusselt number ($Nu_{\theta,c}$), full line for the Nusselt number from the simulation, colors and symbols refer to the considered case.

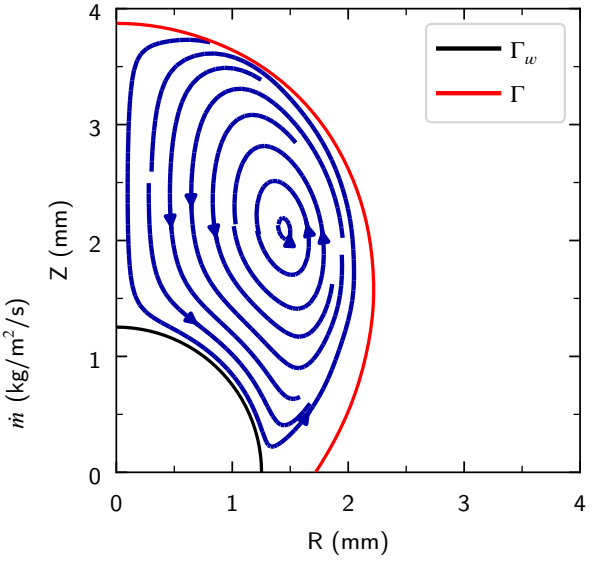

Figure 14: Streamlines for the simulation of a sphere in a subcooled liquid with $Ja_{sup} = 1.51$ at steady state.

vapor film oscillates more in this case than for the others. This may be related to a thicker vapor film leading to a more unstable behavior and to bubble shape oscillations. These oscillations could create more convective heat transfer than simulation with lower Ja_{sub} numbers which could explain higher differences between the Nusselt numbers, Nu_{cond} and Nu, in this case. In Fig. 15, the angular variation of the film thickness $\delta(\theta)$ has been plotted for the lower Ja_{sup} number which is equal to 1.51 and corresponds to the configuration with the thinner film. This figure shows that the film thickness is varying between 75 and 25 µm for angles θ between 0° and ∼ 45° where a pinched zone corresponding to a minimum thickness of the vapor film is observed. Beyond this critical value of θ, the film thickness starts to increase quickly to ∼ 500 µm at $\theta \sim 90°$ and until the final value of ∼ 2.7 mm at $\theta \sim 180°$. This illustrates the

large variation of the film thickness along the sphere with $\delta_{max}/\delta_{min} \sim 100$.

To illustrate this, the velocity field has been plotted at this critical location in Fig.16, for the simulation with Ja_{sup} equal to 1.51. Remarkably, even within this region, the velocity field remains well-resolved thanks to the very refined grid used for these simulations.

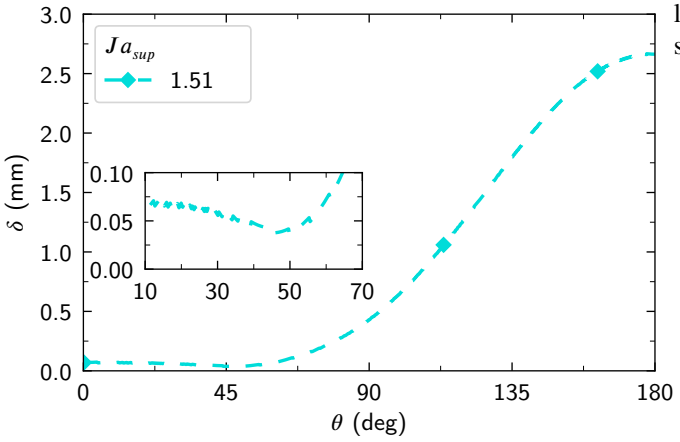

Figure 15: Film thickness as a function of angular coordinate $Ja_{sup} = 1.51$.

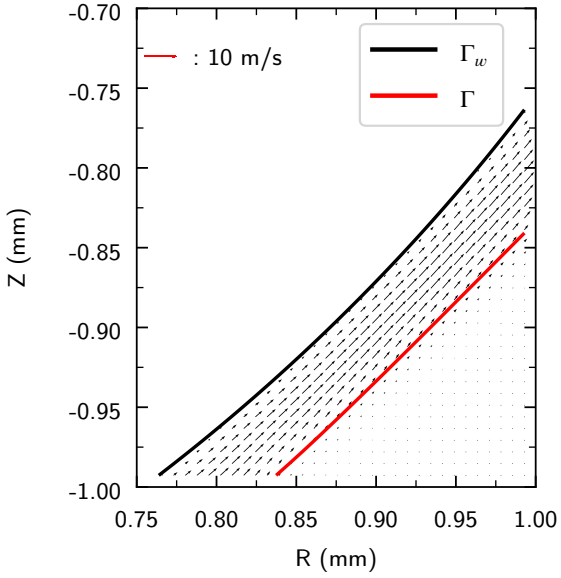

Figure 16: Velocity field at steady state for film boiling around a sphere in a subcooled liquid at the pinched region for $Ja_{sup} = 1.51$.

As previously mentioned, the bubble reaches a steady state due to an equilibrium between vaporization and condensation along its interface. This has been highlighted in Fig. 17 where the dimensionless phase change local mass flow rate, defined as,

$$\tilde{q}_m = \frac{\dot{m} h_{\ell \to v} D}{k_v (T_w - T_{sat})} \tag{31}$$

has been plotted at the interface as a function of the angular coordinate. As expected, vaporization occurs at the bottom of the sphere, until an angle after which condensation begins. This can be attributed to the vapor film thickness which becomes much larger with increasing angular coordinate, as previously observed in Fig. 15. Consequently, beyond a certain angle (approximately 70°), the heat flux originating from the vapor becomes insufficient to sustain vaporization, leading to the onset of condensation induced by the liquid subcooling.

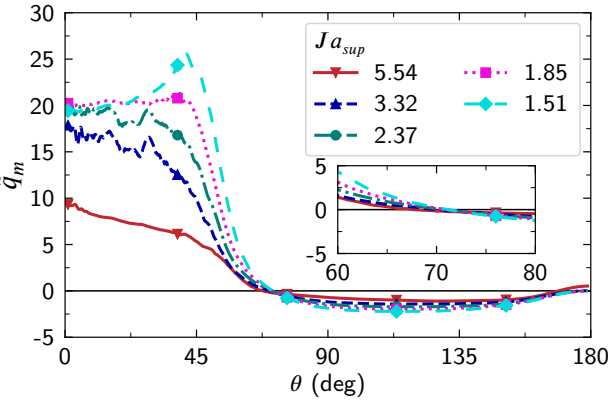

Figure 17: Dimensionless vaporization rate as a function of the angular coordinate for the subcooled film boiling around a sphere at steady state.

Another noteworthy point, in Fig. 17, is $\tilde{q}_m$ that tends to zero on the Z-axis. This can be explained by the formation of a thermal wake at the rear of the bubble in the liquid phase. This thermal wake induces more flattened local temperature gradients than around the bubble, as it can be visualized in Fig. 11(c) and Fig. 11(d), and thus reduces locally the condensation rate to zero. It is worth mentioning that typical values of the condensation rate in Fig. 17 are much lower than values of the vaporization rate. This can be explained by the much lower values of of the Ja_{sub} number than those of Ja_{sup} that are considered in this study. However the overall equilibrium between vaporization and condensation is maintained since condensation occurs on a much larger surface than vaporization.

The velocity profile inside the vapor film is plotted in Fig. 18 at different sections of the bottom part of the vapor film corresponding to the following angles $\theta = 20°, 45°, 70°$, which can be approximately related to the bottom of the sphere, the pinch region, the region where vaporization stops and condensation begins, respectively. In this figure, $\tilde{r}$ is a dimensionless radial coordinate defined as, $\tilde{r} = 2r/D_s - 1$, to ensure a zero-value at the surface of the sphere. This figure shows that a kind of parabolic velocity profile develops in the vapor film, with a maximum velocity which increases with the angular coordinate until reaching the pinched region at $\theta \sim 45°$. The maximum velocity norm diminishes due to the film thickening, although the vapor mass flow rate continues to increase due to vaporization, until reaching the angle $\theta \sim 70°$ after which the vapor mass flow rate will decrease

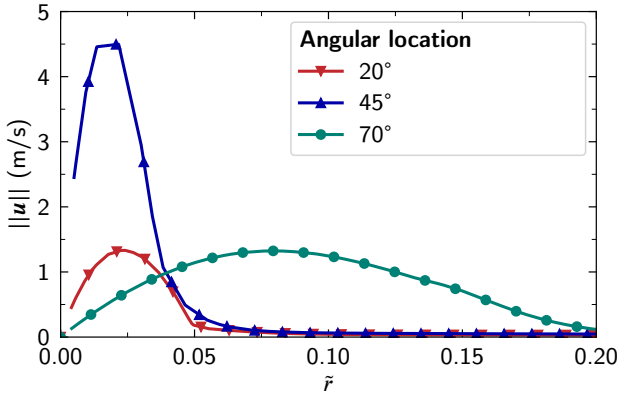

Figure 18: Velocity norm profile at steady state for different angular location for the simulation of subcooled film boiling around a sphere with $Ja_{sup} = 1.51$.

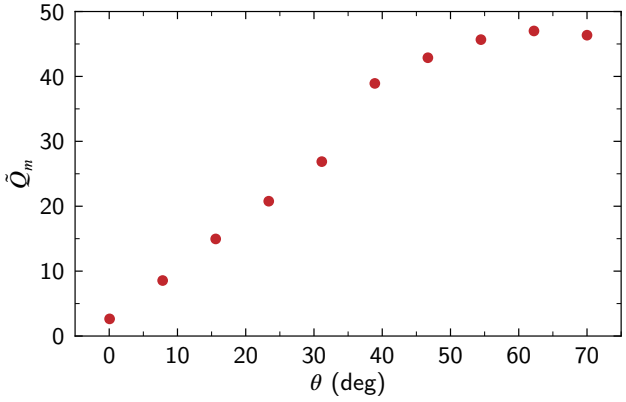

Figure 19: Angular dimensionless vapor mass flow rate in the vapor film for the simulation with $Ja_{sup} = 1.85$ at steady state.

when condensation will occur instead of vaporization. This has been illustrated in Fig. 19, where is plotted the angular variation of the dimensionless total vapor mass flow rate $\tilde{Q}_m$ inside the film, defined as,

$$\tilde{Q}_m = Q_m \frac{h_{\ell \to v}}{k_v (T_w - T_{sat}) D}, \tag{32}$$

with Q_m the dimensional mass flow rate across a section of the vapor film S_f,

$$Q_m = \iint_{S_f} \rho_v \boldsymbol{u} \cdot \boldsymbol{n}_{S_f} dS_f, \tag{33}$$

$\boldsymbol{n}_{S_f}$ being the normal at the surface S_f. This highlights the increase of the vapor mass flow rate inside the film until an angle $\theta \sim 70°$ after which it tends to stabilize or slightly decrease. At approximately 35°, the dimensionless mass flow rate increases quickly. This is related to the vapor film pinch which occurs at this angle for this simulation. Indeed, a decrease of the vapor film thickness leads to an increase of the local vaporization mass flow rate.

To finalize this study, we present in Fig. 20 the evolution of the total Nusselt number with Ja_{sup} and of the dimensionless bubble volume, defined as $\tilde{V}_b = V_b/V_s$, where V_b and V_s are respectively the volume of the bubble and of the sphere. The volume ratio for the simulation with $Ja_{sup} = 5.54$ has not been plotted because during this particular simulation, the thick vapor film exhibited significant oscillations, moving repeatedly from the bottom to the top of the sphere. These oscillations caused considerable fluctuations in the vapor volume throughout the simulation, making it challenging to accurately define and compute the vapor volume for this specific case.As expected, the Nusselt number decreases with an increasing superheated Jakob number. Indeed, lower latent heat (resulting in higher superheated Jakob numbers) implies a thicker vapor film, and thus a lower local heat flux. Since the primary mode of heat transfer in the film boiling process is conduction, a thicker vapor film corresponds to a lower Nusselt number. As well as the Nusselt number, $\tilde{V}_b$ also decreases with Ja_{sup}, if $Ja_{sup} < 3$, but tends to a stabilized value around 4, for higher Ja_{sup}. It is noteworthy that variations of the Ja_{sup} has been obtained by varying the latent heat, which, consequently, also varies Ja_{sub}. This should favor both vaporization in the vaporization region and condensation in the condensation region. This could explain the stabilized value of $\tilde{V}_b$ for increasing values of Ja_{sup}, as a linear compensation between vaporization and condensation.

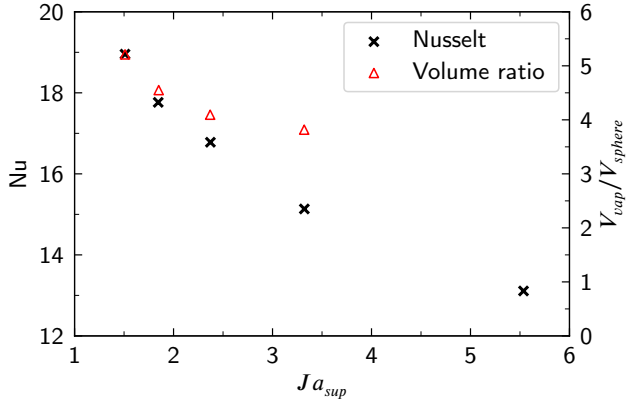

Figure 20: Total Nusselt number and volume ratio between the vapor and the sphere volume as a function the superheated Jakob number for the film boiling simulation around a sphere in a subcooled liquid.

5. Conclusion

To conclude, we have presented in this study a numerical investigation of film boiling in a subcooled liquid around a sphere. Our numerical framework incorporated a low Mach number variable density solver for the vapor phase coupled to an Immersed Boundary Method in a film boiling solver. After preliminary validations a parametric study has been conducted by considering a wide range of latent heat values, resulting in varying superheated and subcooled Jakob

numbers (Ja_{sup} and Ja_{sub}). The simulation domain and boundary conditions were carefully designed to capture the essential features of film boiling around a sphere in subcooled liquid. Our numerical approach adopted a mesh size of 2048×4096 to ensure convergence, and simulations were run until a quasi-steady equilibrium was achieved between vaporization and condensation. The results of our study revealed several key insights. First, as expected, we observed a decrease in the Nusselt number with increasing superheated Jakob number. Higher latent heat (and lower superheated Jakob number) led to a thinner vapor film, resulting in higher Nusselt numbers. Local distribution of the Nusselt number indicated that the heat transfer rate is higher at the bottom of the sphere where the vapor film is thinner due to buoyancy forces. We also verified the well-established hypothesis that conduction is the dominant mode of heat transfer in film boiling. Comparisons between Nusselt numbers computed from our simulations and purely conductive Nusselt numbers confirmed this hypothesis, especially at the bottom of the sphere. Analyzing the equilibrium between vaporization and condensation processes, we found that vaporization primarily occurred at the bottom of the sphere, while condensation begins at around 70°. This behavior was attributed to changes in the vapor film thickness with angular position. This parametric study of film boiling around spheres in subcooled liquid provides new insight on heat transfer and dynamical effect and contributes to a deeper understanding of film boiling phenomena under high superheat conditions and subcooled liquid, with potential applications in various engineering fields. Future works may involve further refinement of the numerical model and exploring additional factors affecting film boiling such as surface characteristics and more extensive parametric studies accounting for other dimensionless numbers. In the framework of this study, our analysis has been restricted to laminar flows and thus to small solid objects, typically millimetered size. This allowed us to perform numerical simulations in 2D coordinates for the horizontal cylinder or in axisymmetric coordinates for the sphere immersed in a subcooled liquid. Indeed, to capture thermal and dynamical effects inside a thin vapor layer, as well as the film shape around the solid object, very refined grids were required. However, even if only small solid objects were considered in this study, many important information and physical insights on film boiling around solid objects have been highlighted on such configurations. Future works considering larger solid objects and possibly 3D turbulent flows will require huge computational resources and a suited adaptive mesh refinement strategy.

Acknowledgments

The authors acknowledge for the financial support of the french government and BPI France in the framework of France Relance 2020-2023 for the project French Fab n° DOS0152116 in collaboration with Framatome.

References

S. Nukiyama, The maximum and minimum values of the heat Q transmitted from metal to boiling water under atmospheric pressure, International Journal of Heat and Mass Transfer 9 (1966) 1419–1433. Number: 12.

L. Bromley, Heat transfer in stable film boiling, volume 46 of *Chemical Engineering Progress*, 1950.

L. A. Bromley, N. R. LeRoy, J. A. Robbers, Heat transfer in forced convection film boiling, Industrial & Engineering Chemistry 45 (1953) 2639–2646. Number: 12 Publisher: ACS Publications.

P. J. Berenson, Film-Boiling Heat Transfer From a Horizontal Surface, Journal of Heat Transfer 83 (1961) 351–356.

V. V. Klimenko, Film boiling on a horizontal plate — new correlation, International Journal of Heat and Mass Transfer 24 (1981) 69–79. Number: 1.

R. D. Cess, E. M. Sparrow, Film Boiling in a Forced-Convection Boundary-Layer Flow, Journal of Heat Transfer 83 (1961a) 370–375. Number: 3.

R. D. Cess, E. M. Sparrow, Subcooled Forced-Convection Film Boiling on a Flat Plate, Journal of Heat Transfer 83 (1961b) 377–379. Number: 3.

M. Epstein, G. M. Hauser, Subcooled forced-convection film boiling in the forward stagnation region of a sphere or cylinder, International Journal of Heat and Mass Transfer 23 (1980) 179–189. Number: 2.

V. K. Dhir, G. P. Purohit, Subcooled film-boiling heat transfer from spheres, Nuclear Engineering and Design 47 (1978) 49–66. Number: 1.

A. Sakurai, M. Shiotsu, K. Hata, Correlations for subcooled pool film boiling heat transfer from large surfaces with different configurations, Nuclear Engineering and Design 120 (1990) 271–280. Number: 2.

M. Shiotsu, K. Hama, Film boiling heat transfer from a vertical cylinder in forced flow of liquids under saturated and subcooled conditions at pressures, Nuclear Engineering and Design 200 (2000) 23–38. Number: 1.

G. Son, V. Dhir, Numerical simulation of saturated film boiling on a horizontal surface (1997).

G. Son, V. K. Dhir, Numerical simulation of film boiling near critical pressures with a level set method (1998).

S. Osher, J. A. Sethian, Fronts propagating with curvature-dependent speed: Algorithms based on Hamilton-Jacobi formulations, Journal of Computational Physics 79 (1988) 12–49. Number: 1.

M. Sussman, P. Smereka, S. Osher, A Level Set Approach for Computing Solutions to Incompressible Two-Phase Flow, Journal of Computational Physics 114 (1994) 146–159.

D. Juric, G. Tryggvason, Computations of Boiling Flows, International Journal of Multiphase Flow 24 (1998) 387–410.

S. W. J. Welch, T. Rachidi, Numerical Computation of Film Boiling Including Conjugate Heat Transfer, Numerical Heat Transfer, Part B: Fundamentals 42 (2002) 35–53. Number: 1 Publisher: Taylor & Francis _eprint: https://doi.org/10.1080/10407790190053824.

R. P. Fedkiw, T. Aslam, B. Merriman, S. Osher, A Non-oscillatory Eulerian Approach to Interfaces in Multimaterial Flows (the Ghost Fluid Method), Journal of Computational Physics 152 (1999) 457–492. Number: 2.

F. Gibou, L. Chen, D. Nguyen, S. Banerjee, A Level-Set based sharp interface method for the multiphase incompressible Navier-Stokes equations with phase change., J Comput Phys 222 (2007) 536–555.

G. Son, V. K. Dhir, A level set method for analysis of film boiling on an immersed solid surface, Numerical Heat Transfer, Part B: Fundamentals 52 (2007) 153–177. Publisher: Taylor & Francis.

G. Son, V. K. Dhir, Three-dimensional simulation of saturated film boiling on a horizontal cylinder, International Journal of Heat and Mass Transfer 51 (2008) 1156–1167. Publisher: Elsevier.

N. K. Singh, B. Premachandran, Mixed regime of film boiling over a horizontal cylinder in an upward flow of saturated liquid, Physics of Fluids 30 (2018) 122101. Number: 12 Publisher: American Institute of Physics.

S. Tanguy, M. Sagan, B. Lalanne, F. Couderc, C. Colin, Benchmarks and numerical methods for the simulation of boiling flows, Journal of Computational Physics 264 (2014) 1–22.

G. Huber, S. Tanguy, M. Sagan, C. Colin, Direct numerical simulation of nucleate pool boiling at large microscopic contact angle and moderate

Jakob number, International Journal of Heat and Mass Transfer 113 (2017) 662–682.

A. Urbano, S. Tanguy, C. Colin, Direct numerical simulation of nucleate boiling in zero gravity conditions, International Journal of Heat and Mass Transfer 143 (2019) 118521.

A. Orazzo, S. Tanguy, Direct numerical simulations of droplet condensation, International Journal of Heat and Mass Transfer 129 (2019) 432–448.

R. Alis, S. Tanguy, K. Kentheswaran, O. Rouzaud, J.-L. Estivalezes, Heat flux and forces acting on a vaporising droplet in a superheated vapor flow, Int J Multiphase Flows 167 (2023) 104526.

G. Mialhe, S. Tanguy, L. Tranier, E.-R. Popescu, D. Legendre, An extended model for the direct numerical simulation of droplet evaporation. influence of the marangoni convection on leidenfrost droplet, J Comput Phys (2023) 112366.

R. B. Pember, L. H. Howell, J. B. Bell, P. Colella, W. Y. Crutchfield, W. A. Fiveland, J. P. Jessee, An Adaptive Projection Method for Unsteady, Low-Mach Number Combustion, Combustion Science and Technology 140 (1998) 123–168.

V. Daru, P. Le Quéré, M.-C. Duluc, O. Le Maître, A numerical method for the simulation of low Mach number liquid–gas flows, Journal of Computational Physics 229 (2010) 8844–8867. Number: 23.

Y. T. Ng, C. Min, F. Gibou, An efficient fluid–solid coupling algorithm for single-phase flows, J Comp Phys 228 (2009) 8807–8829.

I. U. Vakarelski, J. O. Marston, D. Y. C. Chan, S. T. Thoroddsen, Drag Reduction by Leidenfrost Vapor Layers, Physical Review Letters 106 (2011) 214501. Number: 21.

M. Jemison, M. Sussman, M. Arienti, Compressible, multiphase semi-implicit method with moment of fluid interface representation, J Comput Phys 279 (2014) 182–217.

D. Fuster, S. Popinet, An all-mach method for the simulation of bubble dynamics problems in the presence of surface tension, J Comput Phys 374 (2018) 752–768.

A. Urbano, M. Bibal, S. Tanguy, A semi implicit compressible solver for two-phase flows of real fluids., J Comput Phys 456 (2022) 111034.

R. Borges, M. Carmona, B. Costa, W. S. Don, An improved weighted essentially non-oscillatory scheme for hyperbolic conservation laws, Journal of Computational Physics 227 (2008) 3191–3211. Number: 6.

R. P. Fedkiw, A. Marquina, B. Merriman, An Isobaric Fix for the Overheating Problem in Multimaterial Compressible Flows, Journal of Computational Physics 148 (1999) 545–578. Number: 2.

F. Gibou, L. Chen, D. Nguyen, S. Banerjee, A level set based sharp interface method for the multiphase incompressible Navier–Stokes equations with phase change, Journal of Computational Physics 222 (2007) 536–555. Number: 2.

L. Rueda Villegas, R. Alis, M. Lepilliez, S. Tanguy, A Ghost Fluid/Level Set Method for boiling flows and liquid evaporation: Application to the Leidenfrost effect, Journal of Computational Physics 316 (2016) 789–813.

F. Gibou, R. P. Fedkiw, L.-T. Cheng, M. Kang, A Second-Order-Accurate Symmetric Discretization of the Poisson Equation on Irregular Domains, Journal of Computational Physics 176 (2002) 205–227. Number: 1.

D. Q. Nguyen, R. P. Fedkiw, M. Kang, A Boundary Condition Capturing Method for Incompressible Flame Discontinuities, Journal of Computational Physics 172 (2001) 71–98.

T. D. Aslam, A partial differential equation approach to multidimensional extrapolation, Journal of Computational Physics 193 (2004) 349–355. Number: 1.

Y. T. Ng, C. Min, F. Gibou, An efficient fluid–solid coupling algorithm for single-phase flows, Journal of Computational Physics 228 (2009) 8807–8829. Number: 23.

M. Lepilliez, E. R. Popescu, F. Gibou, S. Tanguy, On two-phase flow solvers in irregular domains with contact line, Journal of Computational Physics 321 (2016) 1217–1251.

J. E. Dendy, Black box multigrid, Journal of Computational Physics 48 (1982) 366–386. Number: 3.

L. Torres, A. Urbano, C. Colin, S. Tanguy, On the coupling between direct numerical simulation of nucleate boiling and a micro-region model at the contact line, J Comput Phys 497 (2024) 112602.

L. Rueda Villegas, S. Tanguy, G. Castanet, O. Caballina, F. Lemoine, Direct numerical simulation of the impact of a droplet onto a hot surface above the Leidenfrost temperature, International Journal of Heat and Mass Transfer 104 (2017) 1090–1109.

K. Kentheswaran, N. Dietrich, S. Tanguy, B. Lalanne, Direct numerical simulation of gas-liquid mass transfer around a spherical contaminated bubble in the stagnant-cap regime., International Journal of Heat and Mass Transfer 198 (2022) 123325.

A. Dalmon, M. Lepilliez, S. Tanguy, A. Pedrono, B. Busset, H. Bavestrello, J. Mignot, Direct numerical simulation of a bubble motion in a spherical tank under external forces and microgravity conditions, J. Fluid Mech. 849 (2018) 467–497.

A. Dalmon, M. Lepilliez, S. Tanguy, R. Alis, E.-R. Popescu, R. Roumiguié, T. Miquel, B. Busset, H. Bavestrello, J. Mignot, Comparison between the fluidics experiment and direct numerical simulations of fluid sloshing in spherical tanks under microgravity conditions, Microgravity Sci and Technol 31, issue 1 (2019) 123–138.

Atayılmaz, Teke, Experimental and numerical study of the natural convection from a heated horizontal cylinder, International Communications in Heat and Mass Transfer 36 (2009) 731–738. Number: 7.

E. W. Lemmon, R. T. Jacobsen, S. G. Penoncello, D. G. Friend, Thermodynamic Properties of Air and Mixtures of Nitrogen, Argon, and Oxygen From 60 to 2000 K at Pressures to 2000 MPa, Journal of Physical and Chemical Reference Data 29 (2000) 331–385. Number: 3 Publisher: American Institute of Physics.

E. W. Lemmon, R. T. Jacobsen, Viscosity and Thermal Conductivity Equations for Nitrogen, Oxygen, Argon, and Air, International Journal of Thermophysics 25 (2004) 21–69. Number: 1.

T. H. Kuehn, R. J. Goldstein, Numerical solution to the Navier-Stokes equations for laminar natural convection about a horizontal isothermal circular cylinder, International Journal of Heat and Mass Transfer 23 (1980) 971–979. Number: 7.

H. Ma, L. He, Large eddy simulation of natural convection heat transfer and fluid flow around a horizontal cylinder, International Journal of Thermal Sciences 162 (2021) 106789.

J.-H. Heo, M.-S. Chae, B.-J. Chung, Influences of vertical and horizontal pitches on the natural convection of two staggered cylinders, International Journal of Heat and Mass Transfer 57 (2013) 1–8. Number: 1.

G. Sebastian, S. R. Shine, Natural convection from horizontal heated cylinder with and without horizontal confinement, International Journal of Heat and Mass Transfer 82 (2015) 325–334.

I. U. Vakarelski, J. O. Marston, Y. Chan Derek, S. T. Thoroddsen, Drag reduction by leidenfrost vapor layers, Phys Rev Letters 106 (2011) 214501.

M. Bibal, M. Deferrez, S. Tanguy, A. Urbano, A compressible solver for two phase-flows with liquid-vapour phase change for bubble cavitation, Accepted for publication in J Comput Phys (2024).